Entropic crystal–crystal transitions of Brownian squares

Kun Zhao[a,b], Robijn Bruinsma[a,c], and Thomas G. Mason[a,b,c,1]

[a]Department of Physics and Astronomy, [b]Department of Chemistry and Biochemistry, and [c]California NanoSystems Institute, University of California, Los Angeles, CA 90095

Edited by Tom C. Lubensky, University of Pennsylvania, Philadelphia, PA, and approved December 28, 2010 (received for review October 5, 2010)

When a monolayer of hard microscale square platelets, produced lithographically, is osmotically concentrated in a flat plane to raise the particle area fraction ϕ_A, an order–order transition occurs between a hexagonal rotator crystal and a rhombic crystal. Strikingly, phases having fourfold symmetry are not observed at any ϕ_A. The rhombic lattice angle α increases continuously with ϕ_A, as the system maximizes its total rotational and translational entropy. A cage model, based on packing rotationally swept squares, or "squaroids," reasonably predicts the measured $\alpha(\phi_A)$, indicating that rotational entropy and the square particle shape combine to produce the rhombic unit cell.

colloid | phase behavior | structure | two dimensions | thermal fluctuations

Thermodynamic structures of liquid crystalline mesophases depend in an important way on the geometrical shapes of their constituent molecules. This shape dependence is particularly clear for hard-core repulsive interactions, because the state having minimum free energy is determined by maximizing the entropy through the available free volume per molecule. For solutions of long hard rods, Onsager first showed that the onset of nematic liquid crystalline order depends on molecular geometry through the excluded volume (1). Molecules in two dimensions (2D) are particularly interesting because their shapes and symmetries can determine whether or not a first-order freezing phase transition is replaced by an intervening mesophase, which exhibits a spatial power-law decay in orientational order but only short-range translational order. For hard disks, a sixfold hexatic phase can interpolate between the isotropic liquid and hexagonal 2D crystalline phases (2–9). For hard squares, Monte Carlo (MC) simulations (10) predict that a high-density crystal phase having square symmetry will melt into a tetratic mesophase having a fourfold orientational order at lower densities: The fourfold symmetries of the square crystal and the tetratic mesophase reflect the underlying symmetry of the constituent square particle. However, no experiments have yet been made on systems of Brownian squares that test these predictions.

Lithographic methods have facilitated the synthesis of uniform particulate dispersions containing shape-designed colloids that can serve as model systems for molecular liquid crystals (11–16). When properly controlled, these customized dispersions can be used to study interesting and fundamental problems of statistical mechanics of dense many-particle systems. Although the 2D phase behavior and jammed states of a thermal system of hard pentagons, which cannot fully tile a plane, have been examined (17), a very different set of phases and phase transitions could be observed by investigating a system of Brownian squares which can fully tile a plane.

To investigate this, we have explored the phase behavior of a model aqueous dispersion of lithographic square platelets (i.e., "squares") that diffuse in a plane. We form a monolayer of microscale squares near the bottom surface of a rectangle optical cuvette using roughness-controlled depletion attractions (see *Materials and Methods*) (18, 19); the squares are osmotically compressed in 2D by slightly tilting the cuvette about its long axis. Because the particles have a higher mass density than water, the osmotic pressure Π at a given location in the monolayer arises from the effective gravitational mass of particles above it, projected along the tilted plane. After equilibration, Π increases toward the lower regions of the monolayer, so the particle area fraction ϕ_A also increases, yielding a slowly varying gradient in ϕ_A within the monolayer. Everywhere within the monolayer, Brownian fluctuations are present and drive diffusive dynamics. By examining different locations in the monolayer microscopically, we observe a disorder–order transition as an isotropic phase (I) solidifies into a hexagonal rotator crystal phase (RX) in which the squares can still fully rotate. At larger ϕ_A, we find a phase-coexistence region (CE) that contains crystallites of RX and of a rhombic crystal phase (RB), indicative of a large first-order phase transition. This CE region is followed by a pure RB phase in which the full rotation of the squares is inhibited by neighbors. The RB phase exhibits a continuously changing lattice angle $\alpha(\phi_A)$ and approaches a square phase (SQ) only as ϕ_A increases toward unity. Our observations are strikingly different than MC predictions: RX and RB phases replace the tetratic and square phases seen in MC simulations, and neither RX nor RB directly reflects the square symmetry of the platelets. To understand the origin of the differences, we present a simple mean-field theory of structural phase transitions for 2D excluded-volume crystals based on entropy maximization of a lattice of rotationally swept "squaroids," revealing the importance of rotational entropy in the phase behavior.

Results

In Fig. 1, we show optical micrographs of example configurations of dense thermal squares [*Insets*, Fourier transforms (FTs)]. For $\phi_A \leq 0.60$, an I phase is found (Fig. 1*A*, $\phi_A = 0.52$). As ϕ_A is increased, a disorder–order transition occurs, and a pure RX phase forms (Fig. 1*B*, $\phi_A = 0.62$); hexagonal translational order is evident from the peaks in the FT. A hexatic phase (3–9) potentially exists between I and RX phases, but the limited spatial dynamic range of our observation precludes a definitive identification. As ϕ_A increases further (Fig. 1*C*, $\phi_A = 0.65$), local crystalline domains of an RB lattice form and coexist with hexagonal RX; squares within these rhombic crystallites exhibit strong orientational correlations. Because of the combination of rhombic and hexagonal features, the FT exhibits six wide peaks separated by about 60°, yet two weaker peaks at higher wavenumbers appear due to the RB crystallites. This combination indicates that a CE region, characteristic of a first-order transition, exists between the pure RX and pure RB phases for $0.64 \leq \phi_A \leq 0.66$. Above CE (Fig. 1*D*; e.g., $\phi_A = 0.74$), a pure low-defect RB phase forms in which the average orientation of squares have a well-de-

Author contributions: K.Z. and T.G.M. designed research; K.Z., R.B., and T.G.M. performed research; K.Z., R.B., and T.G.M. contributed new reagents/analytic tools; K.Z., R.B., and T.G.M. analyzed data; and K.Z., R.B., and T.G.M. wrote the paper.

The authors declare no conflict of interest.

This article is a PNAS Direct Submission.

[1]To whom correspondence should be addressed. E-mail: mason@physics.ucla.edu.

This article contains supporting information online at www.pnas.org/lookup/suppl/doi:10.1073/pnas.1014942108/-/DCSupplemental.

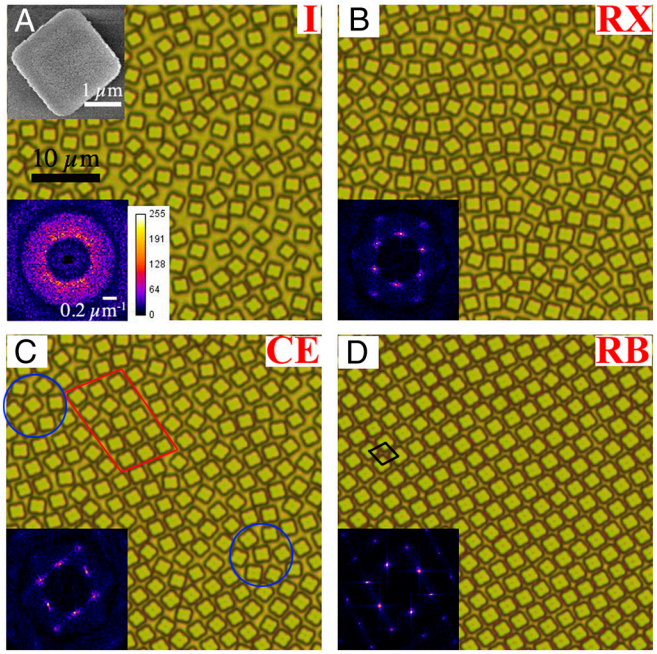

Fig. 1. Transmission optical micrographs of Brownian squares in 2D at particle area fractions ϕ_A: (*A*) 0.52, isotropic (I); (*B*) 0.62, hexagonal rotator crystal (RX); (*C*) 0.65, coexistence (CE); and (*D*) 0.74, rhombic crystal (RB). *Inset*, *Upper Left* corner of *A*: SEM image. *Insets*, *Lower Left* corners: FT intensities calculated from monochrome real-space images. Examples of crystallites in *C*: RB (box) and RX (circles). In *D*, a rhombic unit cell is shown (black rhombus). FTs have been rendered in pseudocolor to emphasize the peak features.

fined angle relative to the crystal axes. The very sharp first- and second-order peaks in the corresponding FT indicate that the rhombic lattice is nearly perfect.

After performing detailed image analysis to determine the center positions and orientations of all squares in a field of view, we calculate the pair correlation function, $g(r/D)$, from a single frame at each ϕ_A. The number of particles over which g is determined ranges from about 350 at $r/D \approx 1$ to about 30 at $r/D \approx 6$, where r is the center-to-center separation between squares and $D = \sqrt{2}L \approx 3.4$ μm is the square's diagonal (i.e., an effective circumscribed diameter) (Fig. 2). As ϕ_A increases above I, the system develops hexagonal translational order in RX, and broadened peaks in $g(r/D)$ are seen to large r/D. The second and third peaks in $g(r/D)$ for RX, characteristic of an equilateral hexagonal crystal, are still distinguishable, yet barely, because of the

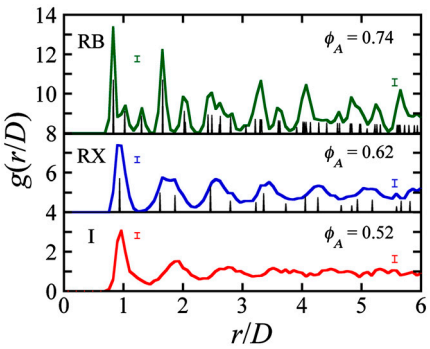

Fig. 2. Pair correlation functions $g(r/D)$ calculated from images in Fig. 1, in order from bottom to top: $\phi_A = 0.52$ in I, 0.62 in pure RX, and 0.74 in pure RB. Results for RX and RB are shifted up for clarity. *D* is the effective tip–tip overlap spacing: $D = \sqrt{2}L \approx 3.4$ μm, where *L* is the square's edge length. Delta spikes for perfect hexagonal and rhombic lattices are shown below the calculated *g* for RX and RB, respectively. Characteristic error bars at certain r/D are shown above each of the respective plots for clarity.

random orientations of the squares and greater variability of center-to-center spacing in RX. In the pure RB phase, the peaks in $g(r/D)$ become quite sharp and can be seen out to very large r/D. Compared to the delta spikes of the ideal $g(r/D)$ for a perfect RB lattice, the measured RB peaks match well. To further confirm our identification of the phases, we have calculated the sixfold spatial and bond-orientational order parameters, as well as the fourfold spatial, bond-orientational, and molecular-orientational order parameters (7–10) (*SI Appendix* provides further details of the analysis).

From the images and FTs, we determine a characteristic lattice angle α and center-to-center spacing r/L of the crystalline phases through the RX–RB transition (Fig. 3). In the CE region, we first isolate and identify crystallites as either RX or RB, and then obtain average values of α and r/L for each type of crystallite. In the hexagonal RX phase, $\alpha \approx 60°$, followed by a discontinuous transition to an angle of about $\alpha \approx 70°$ in the RB phase near the boundary with CE at $\phi_A \approx 0.66$. Likewise, in the CE phase, squares in RB crystallites are closer together than squares in RX crystallites, indicating ϕ_A-density fluctuations and yielding bivalued r/L, characteristic of a first-order transition. Above CE in pure RB, large single crystals are observed, α increases continuously toward 90°, and r/L decreases continuously toward one, up to the highest ϕ_A observed.

To explain some basic aspects of these observations, we introduce a cage-like (20) mean-field model for a monolayer of N square rigid rotors. In I and RX phases, these rotors can perform complete rotations; by contrast, in the RB phase, the rotations are constrained on average within an interval $\pm\Delta\theta/2$, because tip (i.e., vertex) crossing is not allowed. In the RX phase, the swept-out area of each square is a circular disk, which we choose to have unity radius. The area density $\rho = N/A$ for a hexagonal

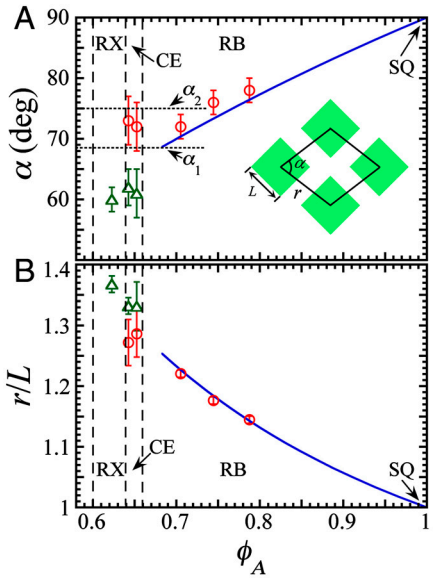

Fig. 3. Particle area fraction dependence of the unit cell for observed crystals of Brownian squares. (*A*) Comparison between measured lattice angles $\alpha(\phi_A)$ (RX, triangles; RB, circles) and predicted values based on a model of squaroid packing (solid line). In the CE region, two measured values of α and r/L are shown, corresponding to characteristics of RX and RB in the observed crystallites. The predicted value α_1 more closely matches the observed angle at the onset of pure RB, compared to an alternate possible configuration given by α_2 (see text). (*Inset*) Sketch of a rhombic unit cell of four squares, defining α, r, and L. (*B*) Center-to-center spacing between squares $r(\phi_A)$ from video analysis, normalized by edge length *L*, compared to the model's predicted dependence (solid line). In the CE region, the lattice angle α and center-to-center spacing r between squares are measured from the direct images; whereas in the RX and RB regions, they are obtained from the Fourier transforms.

configuration of close-packed disks is $\rho_6 = (2\sqrt{3})^{-1}$ (in units of $2/L^2$). For constrained rotations, the excluded area of each square effectively reduces to a cruciform, squaroid shape (Fig. 4*A*). Four distinguishable possible orientations of the square with respect to a given squaroid exist. A close-packed lattice of squaroids retains hexagonal symmetry for $\Delta\theta$ larger than $\pi/3$ (Fig. 4*B*), so the maximum area density remains at ρ_6. However, for $\Delta\theta$ smaller than $\pi/3$, the most compact lattice of squaroids has rhombic symmetry (Fig. 4*C*). At $\Delta\theta = \pi/3$, there is a discontinuous increase in density of close-packed squaroids, and the crystallographic angle α (see Fig. 4*C*) increases from 60° to $\alpha_1 \approx 68°$. As shown in Fig. 3, these two angles and their corresponding area densities are consistent with the two coexisting structures observed in CE.

To describe α at higher area densities, we calculate the 2D osmotic pressure $\Pi = -(dF/dA)|_N$, where A is the total area and F is the entropic free energy. We write F as the sum of a translational free energy $-Nk_BT\ \ln(\rho^{-1} - \rho_{max}^{-1}(\Delta\theta))$, for the translational degrees of freedom, plus a rotational free energy, $-Nk_BT\ \ln(4\Delta\theta)$. For a given $\Delta\theta$, the maximum packing density ρ_{max} equals $1/(2H)$, where H is half of the long diagonal distance in the rhombic unit cell. The corresponding equation of state is $\Pi(\rho) = k_BT\rho/[1 - (\rho/\rho_{max}(\Delta\theta))]$, and the chemical potential, $\mu = F/N + \Pi/\rho$, of the colloids at fixed Π is (up to constant terms)

$$\Delta\mu(\Delta\theta) = -k_BT \ln 4\Delta\theta + \Pi\rho_{max}^{-1}(\Delta\theta), \qquad [1]$$

where $\alpha = 2\arctan(2\rho_{max}(\Delta\theta))$. If, for $\Delta\theta$ less than $\pi/3$, one approximates $\rho_{max}^{-1}(\Delta\theta) \cong 2(1 + \Delta\theta - 0.448\Delta\theta^2 + ...)$, then Eq. **1** resembles the Onsager variational free energy for nematics in terms of $\Delta\theta$. Eq. **1** has a boundary minimum at $\Delta\theta = \pi/3$ corresponding to the rhombic phase of Fig. 4*C*. For $\Pi/k_BT \geq 2.3$, a second "true" minimum appears at $\Delta\theta \approx 0.4$ rad, corresponding to a crystallographic angle $\alpha_2 \approx 75°$. For higher Π, α increases from α_2 toward 90°. The predicted ϕ_A-dependences of α and r/L (lines in Fig. 3 *A* and *B*) are consistent with the experimental observations, despite the simplicity of the model, which completely neglects collective fluctuations.

Discussion

Our observations of Brownian squares reveal RX and RB phases for small dimensionless corner-rounding-to-length ratio ζ; this is at striking variance from the tetratic and square phases predicted by MC simulations for squares with perfectly sharp corners (i.e., $\zeta = 0$) (10). Indeed, after concentrating larger square-shaped particles, for which $\zeta = 0.07 \pm 0.01$ is even smaller (*SI Appendix* provides further details of the analysis), we still observe a rhombic structure at $\phi_A = 0.70$ with $\alpha = 79°$; at the largest applied Π, corresponding to $\phi_A = 0.85$, we find $\alpha = 88°$. With increasing density, α approaches the crystallographic angle of the square phase, but it never fully reaches 90° at finite Π, consistent with the squaroid-mean-field theory (see Fig. 3*A*). Using the method of Fig. 4, it can be shown that any degree of corner-rounding of squares would lead to a stable RB phase, rather than a perfectly square crystal, even at the highest packing density. For even larger ζ approaching 0.5, the rounded squares become nearly circular, and the RB phase is progressively engulfed by the hexagonal RX phase. By contrast to the RB phase, in the RX phase, the squares can rotationally diffuse in an unbounded manner, as can be seen in calculations of the mean square displacements, both rotational and translational, in several different phases (*SI Appendix* provides further details of the analysis).

For certain shapes, feature rounding is known to have a very important effect on collective phase behavior. For instance, in density-functional studies, a tetratic phase appears for rectangles that have sharp corners but not for disco-rectangles that have rounded end-caps (21). In simulations of disco-rectangles having aspect ratios ranging from discs to needles, no tetratic phase was found (22). By contrast, tetratic liquid and solid phases have been seen in simulations of slightly rounded 2:1 rectangles based on superellipses (23). Because a rectangular shape introduces another dimensionless spatial parameter of aspect ratio, in addition to ζ, it is difficult to make an exact comparison between the phases seen in simulations of rounded rectangles and our experiments on slightly rounded squares. In these simulations, corner-rounding does not introduce the oblique crystallographic angles we observed. MC simulations typically impose square boundary conditions, which may suppress structures with oblique crystallographic directions, and it is possible that our experimental system is, in fact, a close enough approximation of ideal Brownian squares that the RX and RB phases would be seen even if the corners could be made perfectly sharp. Indeed, our results imply that the tetratic phase, seen for rectangles, could transition into an ordered RX or RB phase as the length-to-width ratio of the rectangles approaches unity and they become square-shaped. Also, the simulations might not check for vertex crossing events between one state and the next, possibly simulating squares that effectively have "phantom" vertices; in the experiments, vertices are strictly hard and any rare passage of a vertex of a given square by a vertex of a closely neighboring square at high ϕ_A beyond the RX phase appears to be coupled to substantial collective fluctuations. It is very unlikely that the slowly varying gradient in ϕ_A in our observations (e.g., approximately 1% in ϕ_A over about 90 particles along the tilting direction in the pure RB phase) would be the source of differences in the results between the experiments and simulations, because we observe that both RX and RB phases persist over a substantial range of ϕ_A, corresponding to a much larger area than a single field of view.

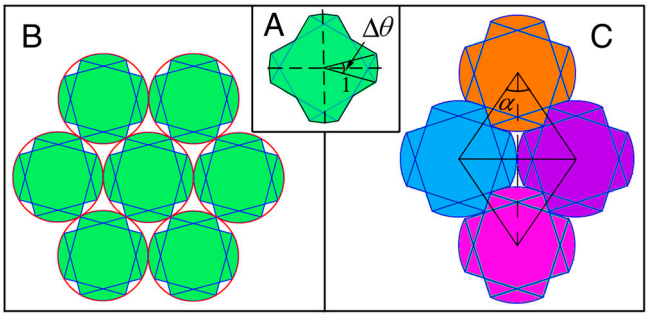

Fig. 4. Squaroid packing model for predicting structure and phase behavior of Brownian squares. (*A*) Rotating a square about its center by $\pm\Delta\theta/2$ produces a squaroid (green). (*B*) Squaroids in a hexagonal RX array at a density just below the transition from RX to RB. Red circles indicate full 2π rotations of the squares in RX. (*C*) Squaroids in an oblique rhombic lattice at higher densities. As shown, α is the rhombic lattice angle. Different colors are used to better distinguish squaroids in the rhombic unit cell.

Conclusion

In conclusion, a Brownian monolayer of hard square colloids has been used to study a fundamental problem in statistical mechanics: a 2D order–order transition at high densities. We have observed a first-order transition from a hexagonal rotator crystal to a rhombic crystal through a coexistence region; the system self-adjusts into a rhombic configuration to maximize the combination of translational and rotational entropy, even as the range of rotation of individual squares becomes limited. The observed transition is consistent with a simple theoretical model based on efficiently packing squaroids whose shapes effectively incorporate rotational entropy over a limited range of accessible angles in the absence of tip crossing. Strikingly, neither observed crystal phase has the simple fourfold symmetry of the constituent square particles. It would be interesting for future simulations and experiments to consider how corner-rounding, tip crossing, and boundary conditions can affect the phase behavior of dense

systems of Brownian hard squares. Moreover, studying the coupling between entropically driven collective translational and rotational fluctuations of the lattice, both theoretically and experimentally, would provide greater insight into the spatiotemporal dynamics beyond the simple cage model.

Materials and Methods

Preparation of Samples. Aqueous dispersions containing many millions of uniform square platelets of SU-8 polymer, having average edge length $L = 2.4 \pm 0.1$ μm and thickness $h = 2.0 \pm 0.1$ μm (Fig. 1*A*, *Inset*), are made using high-fidelity stepper photolithography (15). Due to the stepper's limited feature size (≈300 nm), the corners of the squares are slightly rounded and have an average radius of curvature $r_c = 0.30 \pm 0.05$ μm, yielding a small $\zeta = r_c/L = 0.13 \pm 0.02$. A rectangular optical cuvette (0.2 mm × 4.0 mm × 20 mm) is filled with a mixture of a dilute dispersion of squares and a dispersion of a depletion agent (polystyrene spheres, diameter ≈0.02 μm, concentration ≈0.5% wt/vol, sulfate stabilized). After the squares sediment onto one flat surface of the cuvette, roughness-controlled depletion attractions (18, 19) force the squares to lie flat, parallel to the glass wall; yet, due to a lubricating layer of water, they remain unpinned and diffuse in a monolayer. Because the edges of the squares are rougher than their faces, the effective attraction between two edges is less than thermal energy k_BT; thus, hard, short-range repulsions dominate in-plane particle interactions (see Supplemental Material in ref. 17). Squares are concentrated in 2D by tilting the cuvette about its long axis at angles ≈1° and waiting a minimum of 2 mo for equilibration, creating a slowly varying spatial gradient in ϕ_A. Specific ϕ_A are viewed microscopically along the length of the cuvette, and about 400 particles at high ϕ_A are observed in a single field of view (64 μm × 64 μm).

Image Analysis. We have adapted the particle tracking programs of Crocker and Grier (24), written in Interactive Data Language, to determine not only the positions but also the orientations of a large number of squares in a field of view. After finding the center of a given square, we determine the location of a vertex by looking for the longest distance from the center to the boundary points (*SI Appendix*). From these two coordinates, we determine the line from the center to this vertex as the orientation of the square.

ACKNOWLEDGMENTS. We thank the National Science Foundation (CHE0450022 and DMR 0404507) for partial support.

1. Onsager L (1949) The effects of shape on the interaction of colloidal particles. *Ann NY Acad Sci* 51:627–659.
2. Halperin BI, Nelson DR (1978) Theory of two-dimensional melting. *Phys Rev Lett* 41:121–124.
3. Mak CH (2006) Large-scale simulations of the two-dimensional melting of hard disks. *Phys Rev E* 73:065104.
4. Han Y, Ha NY, Alsayed AM, Yodh AG (2008) Melting of two-dimensional tunable-diameter colloidal crystals. *Phys Rev E* 77:041406.
5. Zahn K, Lenke R, Maret G (1999) Two-stage melting of paramagnetic colloidal crystals in two dimensions. *Phys Rev Lett* 82:2721–2724.
6. Ebert F, Dillmann P, Maret G, Keim P (2009) The experimental realization of a two-dimensional colloidal model system. *Rev Sci Instrum* 80:083902.
7. Murray CA, Winkle DHV (1987) Experimental observation of two-stage melting in a classical two-dimensional screened Coulomb system. *Phys Rev Lett* 58:1200–1203.
8. Strandburg KJ (1988) Two-dimensional melting. *Rev Mod Phys* 60:161–207.
9. Nelson DR (2002) *Defects and Geometry in Condensed Matter* (Cambridge Univ Press, Cambridge, U.K.).
10. Wojciechowski KW, Frenkel D (2004) Tetratic phase in the planar hard square system. *Comp Met Sci Technol* 10:235–255.
11. Love JC, Wolfe DB, Jacobs HO, Whitesides GM (2001) Microscope projection photolithograpy for rapid prototyping of masters with micron-scale features for use in soft lithography. *Langmuir* 17:6005–6012.
12. Hoover MD, et al. (1990) A method for producing non-spherical monodisperse particles using integrated circuit fabrication techniques. *J Aerosol Sci* 21:569–575.
13. Brown ABD, Smith CG, Rennie AR (2000) Fabricating colloidal particles with photolithography and their interactions at an air-water interface. *Phys Rev E* 62:951–960.
14. Sullivan M, et al. (2003) Control of colloids with gravity, temperature gradients, and electric fields. *J Phys Condens Matter* 15:S11–S18.
15. Hernandez CJ, Mason TG (2007) Colloidal alphabet soup: Monodisperse dispersions of shape-designed lithoparticles. *J Phys Chem C* 111:4477–4480.
16. Dendukurl D, Pregibon DC, Collins J, Hatton TA, Doyle PS (2006) Continuous-flow lithography for high-throughput microparticle synthesis. *Nat Mater* 5:365–369.
17. Zhao K, Mason TG (2009) Frustrated rotator crystals and glasses of Brownian pentagons. *Phys Rev Lett* 103:208302.
18. Zhao K, Mason TG (2007) Directing colloidal self-assembly through roughness-controlled depletion attractions. *Phys Rev Lett* 99:268301.
19. Zhao K, Mason TG (2008) Suppressing and enhancing depletion attractions between surfaces roughened by asperities. *Phys Rev Lett* 101:148301.
20. Buehler RJ, Wentorf RH, Hirschfelder JO, Curtiss CF (1951) The free volume for rigid sphere molecules. *J Chem Phys* 19:61–71.
21. Martínez-Ratón Y, Velasco E, Mederos L (2005) Effect of particle geometry on phase transitions in two-dimensional liquid crystals. *J Chem Phys* 122:064903.
22. Bates MA, Frenkel D (2000) Phase behavior of two-dimensional hard rod fluids. *J Chem Phys* 112:10034–10041.
23. Donev A, Burton J, Stillinger FH, Torquato S (2006) Tetratic order in the phase behavior of a hard-rectangle system. *Phys Rev B* 73:054109.
24. Crocker JC, Grier DG (1996) Methods of digital video microscopy for colloidal studies. *J Colloid Interface Sci* 179:298–310.